

HYDRODYNAMIC PHOTOEVAPORATION OF PROTOPLANETARY DISKS WITH CONSISTENT THERMOCHEMISTRY

LILE WANG¹ AND JEREMY J. GOODMAN¹

Draft version November 12, 2018

ABSTRACT

Photoevaporation is an important dispersal mechanism for protoplanetary disks. We conduct hydrodynamic simulations coupled with ray-tracing radiative transfer and consistent thermochemistry to study photoevaporative winds driven by ultraviolet and X-ray radiation from the host star. Most models have a three-layer structure: a cold midplane, warm intermediate layer, and hot wind, the last having typical speeds $\sim 30 \text{ km s}^{-1}$ and mass-loss rates $\sim 10^{-9} M_{\odot} \text{ yr}^{-1}$ when driven primarily by ionizing UV radiation. Observable molecules including CO, OH and H₂O re-form in the intermediate layer and survive at relatively high wind temperatures due to reactions being out of equilibrium. Mass-loss rates are sensitive to the intensity of radiation in energy bands that interact directly with hydrogen. Comparison with previous works shows that mass loss rates are also sensitive to the treatment of both the hydrodynamics and the thermochemistry. Divergent results concerning the efficiency of X-ray photoevaporation are traced in part to differing assumptions about dust and other coolants.

Subject headings: accretion, accretion disks — stars: planetary systems: protoplanetary disks — planets and satellites: formation — circumstellar matter — astrochemistry — method: numerical

1. INTRODUCTION

Protostellar/protoplanetary disks (hereafter PPDs) surrounding low-mass T Tauri stars are the birthplaces of planets and have typical lifetimes $\sim 10^6 - 10^7 \text{ yr}$ lifespan (e.g. Zuckerman et al. 1995; Haisch et al. 2001). Along with accretion onto the star, sequestration of mass in planets, and perhaps magnetized disk winds, photoevaporation by hard photons likely contributes to the dispersal of PPDs (Hollenbach et al. 1994).

Hard photons in different energy bands experience different microscopic physics and have differing effects on PPDs. Following Gorti & Hollenbach (2009), we use the term “far-UV (FUV)” for photon energies $6 \text{ eV} < h\nu < 13.6 \text{ eV}$, “extreme-UV (EUV)” for $13.6 \text{ eV} < h\nu < 0.1 \text{ keV}$, and “X-ray” for $h\nu > 0.1 \text{ keV}$. While EUV may be blocked by the wind from the disk surface (e.g. Alexander et al. 2005), FUV and X-ray radiation are more penetrating. All of these heat, dissociate, or ionize the gas via a plethora of mechanisms. In order to model photoevaporation of PPDs, therefore, one is required to take the richness of the microphysics into account, as well as its interaction with the hydrodynamics.

Evolving a hydrodynamic system coupled with thermochemistry to (quasi-) steady state could be prohibitively expensive if a large chemical reaction network were included. Past work on PPD photoevaporation has compromised (at least) one of the two aspects: hydrodynamics or thermochemistry. Alexander et al. (2006a,b) modeled EUV photoevaporation in hydrodynamic simulations with minimum thermochemistry. On the other hand, calculations with detailed thermochemistry usually adopt semi-analytic prescriptions for the wind mass-loss rate rather than simulate multidimensional hydrodynamics e.g. Gorti & Hollenbach (2008, 2009) (hereafter GH08, GH09). Some recent works conduct hydrody-

amic simulations with interpolation tables for gas temperature drawn from hydrostatic scenarios (e.g. Owen et al. 2010). More recently, Haworth & Harries (2012), Haworth et al. (2016), and Haworth et al. (2017) have coupled hydrodynamics and thermochemistry in simulations of externally irradiated disks and pre-stellar cores; their code is three-dimensional, but their applications have been confined mostly to simplified geometries (spherical or cylindrical) for easier comparison to semi-analytic work.

This work focuses on a consistent combination of hydrodynamic simulation with a moderate-scale chemical network (24 species, $\sim 10^2$ reactions). We include the species and reactions that are relevant to photoevaporation, especially heating and cooling mechanisms. Full hydrodynamic simulations are carried out in 2.5-dimensions (axisymmetry), coupled with radiation, thermodynamics, and chemistry, by solving time-dependent differential equations in every zone throughout the simulation domain. Compared to simulations with interpolation tables for thermochemistry, this approach is able to deal with non-equilibrium processes, as when some chemical and hydrodynamic timescales are comparable. The long-term goal of our exploration is to predict observables, especially emission and absorption-line profiles and strengths of important atomic and molecular species, thereby constraining our wind models and the parameters that go into them (e.g. abundances, dust properties, EUV luminosities). We aim eventually to incorporate MHD processes, and expect that the combination of photoevaporative and magnetic effects will lead to higher mass-loss rates than each process acting alone. The hydrodynamic simulations presented here are first steps toward these goals.

This paper is structured as follows. In §2, we briefly summarize our numerical methods and physical approximations. Additional details concerning our treatment of

¹ Princeton University Observatory, Princeton, NJ 08544

thermochemical processes are given in the Appendices. §3 introduces the parameter choices underlying our fiducial model. §4 presents the main results of our calculations for this model, and for several other models that differ from the fiducial one in one or more parameters, with the goal of exploring the effects of these parameters on gross properties of the flow, especially the mass-loss rate. In §5, we discuss the role that different bands of radiation play, and also compare and contrast our results with those of Gorti & Hollenbach (2009) and Owen et al. (2010). §6 concludes and summarizes the paper.

2. METHODS

This section summarizes our methods. The computational scheme for hydrodynamics is first described, followed by our methods for radiative transfer and thermochemistry.

2.1. Hydrodynamics

Our modeling of PPD photoevaporation systems involves full hydrodynamic calculations. We use the grid-based, general-purpose, astrophysical code **Athena++** (White et al. 2016; Stone et al., in preparation) in spherical coordinates (r, θ, ϕ) but neglect all dependence on ϕ : our simulations are axisymmetric. Magnetic fields are neglected in the present work, although **Athena++** is fully capable of MHD (indeed optimized for it). We use the HLLC Riemann solver and van Leer reconstruction with improved order of accuracy using the revised slope limiter (see Mignone 2014). Consistent Multi-fluid Advection (CMA) is used to ensure strict conservation of chemical elements and species (e.g. Glover et al. 2010).

2.2. Radiative transfer

Absorption processes dominate scattering for most of the radiation that we consider: FUV, EUV, and 1 keV X-rays (Draine 2011; Verner et al. 1996). An exception would be Ly α photons, which may dominate the FUV luminosity, and whose scattering into nonradial directions helps them to penetrate more deeply into the disk (e.g. Bethell & Bergin 2011). We find, however, that unscattered soft FUV photons penetrate the intermediate layer anyway, and more deeply than Ly α . Like Ly α , these photons dissociate H₂O and OH, which can be important coolants, but not H₂ or CO (e.g. Shull 1978). The scattering of harder X-rays can be important for ionization and hence magnetic coupling of the upper layers of the disk (Igea & Glassgold 1999; Bai & Goodman 2009, e.g.), but we are neglecting magnetic fields here.

Therefore, in this paper, scattering is neglected, and radiative transfer consists only of radial ray tracing, the sources of all hard photons being assumed to lie at the origin ($r = 0$). This is facilitated by our choice of spherical coordinates, although our algorithm can trace rays in nonradial directions also (Wang 2017, in preparation).

One ray is assigned to each radial column. Its luminosity is adjusted as it propagates through each cell according to the photoreactions within that cell. Some cells can be individually optically thick. Hence for photochemistry, we adopt as the effective flux at photon frequency ν ,

$$F_{\text{eff}}(\nu) = F_0(\nu) \left\{ \frac{1 - \exp[-\delta l / \lambda(\nu)]}{\delta l / \lambda(\nu)} \right\}, \quad (1)$$

where F_0 is the flux impinging on the inner face of the current cell, $\lambda(\nu)$ is the local absorption mean free path of photons at frequency ν , and δl is the chord length of the ray across the cell. (For radial ray tracing, δl is simply the radial width of the cell.) Eq. (1) yields $F_{\text{eff}} \rightarrow F_0$ as $(\delta l / \lambda) \rightarrow 0$.

2.3. Chemistry and Thermodynamics

In each cell, a coupled set of ordinary differential equations (ODEs) is solved to update the abundances of all \mathcal{N} chemical species $\{n^i\}$ and internal energy density ϵ . These equations read, nominally,

$$\begin{aligned} \frac{dn^i}{dt} &= \mathcal{A}^i_{jk} n^j n^k + \mathcal{B}^i_j n^j; \\ \frac{d\epsilon}{dt} &= \Gamma - \Lambda; \end{aligned} \quad (2)$$

in which the terms involving $\{\mathcal{A}^i_{jk}\}$ describe two-body reactions, while those in $\{\mathcal{B}^i_j\}$ represent photoionization and photodissociation. Γ and Λ are the heating and cooling rates per unit volume, respectively. $\{\mathcal{A}^i_{jk}\}$, Γ and Λ are usually functions of temperature T . The thermal energy density $\epsilon = c_V(\{n^i\})T$, where c_V is the heat capacity of the gas at constant volume. (Thermochemistry and hydrodynamics are solved in separate substeps, whence we use c_V instead of c_P here.) The ODEs (2) are solved in conjunction with the hydrodynamics by operator splitting. That is, they are advanced one time step after each hydrodynamic step, which has included advection of the chemical species, while holding the masses of all elements fixed within each cell. Photoreactions are included using the radiative fluxes computed as described in §2.2. The updated internal energy ϵ and number densities $\{n^i\}$ of all species are then used to initialize the next hydrodynamic step.

The ODEs (2) are usually stiff and hence numerically difficult. We use a standard ODE solver with adaptive implicit modules, **CVODE** (see Hindmarsh et al. 2005). The solution of these equations dominates our total computation time, typically by a factor $\gtrsim 10$ compared to the hydrodynamics. Nonetheless, this brute-force approach rewards us by being able to deal with non-equilibrium conditions, as will be discussed later in this paper.

Guided by GH08, GH09, and our own numerical experiments, we adopt 24 species that are most relevant to heating and cooling processes involved in PPD photoevaporation: e⁻ (free electrons), H⁺, H, H₂, H₂^{*} (using the $v = 6$ vibrational state as a proxy for H₂ in all excited states, see Appendix A.1 and TH85), He, He⁺, O, O⁺, O^{*} (the ¹D state of atomic oxygen as a proxy for all neutral excited states, see Appendix A.2), OH, H₂O, C, C⁺, CO, S, S⁺, Si, Si⁺, Fe, Fe⁺, Gr, Gr⁺, Gr⁻. Here Gr and Gr[±] denote neutral and singly-charged dust grains, respectively.

We extract the reactions involving these species from the UMIST astrochemistry database (McElroy et al. 2013). However, the interstellar radiation fields and matter densities to which the standard UMIST database is usually applied are rather different from those of PPDs. We therefore exclude all reactions involving photons and dust grains in the UMIST library; instead, we evaluate those reaction rates separately.

Photoionization and photodissociation are critical mechanisms that affect photoevaporation. At each photon energy, the ionization cross section of each atomic species is evaluated using the data in Verner & Yakovlev (1995); Verner et al. (1996). For molecular species that can react with FUV photons, namely H_2 , CO , OH , and H_2O here, we adopt the FUV-induced photochemical reaction rate based on Tielens & Hollenbach (1985, hereafter TH85) for H_2 , Visser et al. (2009) for CO (note that this photodissociation cross section is $\sim 10\times$ the value in TH85), and Ádámkóvics et al. (2014, hereafter AGN14) for H_2O and OH . The photochemical processes related to H_2 , C and CO may be subject to considerable self-shielding and cross-shielding. Using the radial column density data that are obtained by integrating along radial rays, we evaluate the impact of the self-/cross-shielding by adopting the analytic formulae in Visser et al. 2009 (for CO) and TH85 (for C), and Draine & Bertoldi (1996) (for H_2). It is worth noting that the FUV-induced processes in parallel with photodissociation of H_2 , H_2O and OH , e.g. FUV pumping of H_2 onto its excited states and its subsequent effects, can have considerable thermodynamic effects. We refer the reader to Appendices A.1 and A.2 for detailed discussion.

Heating and cooling processes are directly associated with chemical reactions. While the amount of energy deposited into and removed from the gas by photoionization and recombination can be estimated straightforwardly (see also Draine 2011, eqs. 27.3, 27.23), the thermodynamic effects of other chemical reactions need elaboration, which is provided in Appendices A.1 through A.3. There are other radiative mechanisms that remove energy from the gas, especially collisionally pumped rovibrational transitions of molecules, and fine-structure transitions of atoms. We briefly summarize those mechanisms and our method for evaluating them in Appendix A.4.

Dust grains are usually crucial in PPD photoevaporation. Following the arguments in GH08, as well as Geers et al. (2006, 2007); Perez-Becker & Chiang (2011), we suggest that polycyclic aromatic hydrocarbons (PAHs) overwhelm dust grains of other sizes in terms of the following effects, thanks to their dominant contribution to total dust surface area: photoelectric heating of gas, dust-gas collisional energy transfer, recombination with free electrons, dust-assisted molecular hydrogen formation, and neutralization of positive ions. We include the processes listed above as outlined in Appendix A.3.

3. CHOICE OF FIDUCIAL MODEL

This section presents the setup of our fiducial model, whose main properties are listed in Table 1. Other models, each differing from the fiducial in one parameter, are described in §4.2.

The simulation domain is axisymmetric, extending from 2 AU to 100 AU in radius (r) and 0 to $\pi/2$ in colatitude (θ). All models are presumed to be symmetric about the equatorial plane, so that, for example, quoted mass-loss rates include outflows at $\theta > \pi/2$. All dependence on the azimuthal coordinate (ϕ) is ignored. Outflow boundary conditions with a radial flow limiter (which inhibits radial inflow) are imposed at $r = 2$ AU and $r = 100$ AU, and reflecting boundary conditions at $\theta = 0$ and $\theta = \pi/2$. Our standard resolution is 256 radial by 128 latitudinal

zones, the radial zones being logarithmically spaced, and the latitudinal zones equally spaced.

The gravitational field is that of a $1 M_\odot$ star located at the origin. The disk, whose self-gravity is neglected, is initialized in hydrostatic and centrifugal balance, except for slight imbalances due to numerical discretization. The disk density and temperature profile follow the steady state solution in Nelson et al. (2013), in which we set the midplane density as $n = 10^{10} \text{ cm}^{-3}$ and temperature $T = 20 \text{ K}$ at $r = 10^2 \text{ AU}$, with radial power index being (-2.25) for density and (-0.5) for temperature—this profile yields a disk mass $\approx 0.03 M_\odot$ within 100 AU. The density and temperature profiles roughly agree with GH09, but the latter are not quite hydrostatic.

All radiation emanates from the origin of spherical polar coordinates. Our simulation domain does not cover the origin, and the rays are not attenuated before they reach the inner boundary. The source is isotropic, but those rays that reach the midplane region at the inner boundary are discarded (we also test not discarding those rays, finding negligible differences in the dissociation layer and in the wind). Each ray has four discrete energy bins, representing four important bands of photon energy: $h\nu = 7 \text{ eV}$ for FUV photons that do not interact appreciably with hydrogen molecules (“soft FUV” hereafter), 12 eV for Lyman-Werner (“LW” for short) band photons, 25 eV for EUV photons, and 1 keV for X-ray photons. $\text{Ly}\alpha$ photons are neglected, as discussed above. The number of photons radiated in each energy bin per unit time follows the luminosity model described in GH08 and GH09: (1) a 9000 K black body spectral profile for FUV ($6 \text{ eV} < h\nu < 13.6 \text{ eV}$) with total luminosity $L_{\text{FUV}} = 10^{31.7} \text{ erg s}^{-1}$; (2) an additional EUV-photon emission rate $^2 \Phi_{\text{EUV}} = 10^{40.7} \text{ s}^{-1}$; (3) and an X-ray luminosity $L_X = 10^{30.4} \text{ erg s}^{-1}$.

The initial elemental abundances are determined by the values in Table 1 (wherein n_{H} is the number density of hydrogen nuclei). These choices generally follow a subset of those in GH08, with the additional assumption that elements appear in chemical compounds if possible. These initial abundances are uniform throughout the simulation domain.

Our assumptions about the dust turn out to be important for our results. GH08 and GH09 treated two populations of grains: (i) an MRN-type power-law distribution with a minimum grain radius of 50 \AA , maximum of $20 \mu\text{m}$, and a dust-to-gas ratio by mass of 10^{-2} ; and (ii) PAH grains with abundance 8.4×10^{-8} per hydrogen nucleus. The first population has a total geometrical cross section of $2 \times 10^{-22} \text{ cm}^2$ per hydrogen nucleus ($\sigma_{\text{dust}}/\text{H}$). The authors do not state the radius of their PAH grains explicitly, but they refer to Li & Draine (2001), and we interpret this to mean that their PAHs can be approximated by spheres of radius 6 \AA . It would follow that the contribution of their PAHs to the cross section is $\sigma_{\text{dust}}/\text{H} \approx 9.5 \times 10^{-22}$, i.e. several times larger than that of their MRN population, although the contribution to the dust-to-gas mass ratio is only $\sim 10^{-4}$. As noted above, A.3, the principal effects of dust, especially heating and absorption of radiation, are expected to be

² GH08 and GH09 assumed different EUV luminosities for their fiducial models. Here we adopt the value specified in GH09.

dominated by the smallest grains—PAHs.

For simplicity, we prefer to work with a single-sized grain population. We therefore neglect MRN grains and take the approximate relative abundance for our PAH-like grain species (Gr) as 10^{-7} per hydrogen atom, slightly greater than that of GH08, and a PAH radius of 5 Å, i.e. approximately 60 carbon atoms per PAH: see Weingartner & Draine 2001). The dust-to-gas mass ratio is then 0.7×10^{-4} , and $\sigma_{\text{dust}}/H = 8 \times 10^{22} \text{ cm}^2$.

Although variable dust abundance is fully allowed by our code, for the sake of simplicity we set the relative abundance of Gr to be uniform and assume that the dust comoves with the gas.

We run the simulation for 1.2×10^4 yr with microphysics enabled but the central radiation sources turned off until the disk structure is fully numerically relaxed, and the temperature profile converges to that set by the artificial heating profile (§A.3.3, which is sufficiently close to the initial profile. The chemical abundances do not change during this relaxation process except by passive advection. We confirm after this process that the disk is indeed in hydrodynamic equilibrium and has no outflow. Then, at $t = 3.6 \times 10^3$ yr, irradiation is turned on and remains on for the rest of simulation; this lasts $\gtrsim 500$ yr, sufficiently long compared to the radial flow timescale $\tau \sim (100 \text{ AU})/(30 \text{ km s}^{-1}) \approx 16$ yr so as to reach an approximate quasi-steady state. On Princeton University’s local computer cluster *perseus*, 500 yr of simulated time takes ~ 100 hrs of wall-clock time on 128 CPUs. About 95 per cent of the time is consumed by the thermochemical calculations for the fiducial model, the hydrodynamic and ray-tracing steps being relatively quick.

We also calculate several models that differ from the fiducial in one or more parameters, as described in §4.2.

4. RESULTS

In this section, we first present and elaborate the fiducial simulation (see §3), then compare the the results of the variant models shown in 2 (see §4.2).

4.1. Fiducial Model

Fig. 1 displays meridional plots of the structure of our fiducial model averaged over the final 100 yr of the simulation. The white curves shown in the top row of panels are streamlines, the integral curves of the vector field $\rho \mathbf{v}_p$ (\mathbf{v}_p is the poloidal velocity), spaced by constant mass-loss rate $10^{-10} M_{\odot} \text{ yr}^{-1}$: that is to say, this is the mass flux between neighboring streamlines when integrated over azimuth and multiplied by two to include the reflection of the computational region below the equatorial plane. Streamlines that meet the outer boundary with a negative value of the Bernoulli parameter

$$\mathcal{B} \equiv \frac{v^2}{2} + \frac{\gamma p}{(\gamma - 1)\rho} + \Phi, \quad (3)$$

are not plotted, and the outflow along such streamlines is omitted from the computation of the total mass-loss rate. Here v is the magnitude of fluid velocity vector, p the gas pressure, $\gamma \approx 5/3$ the adiabatic index, and Φ the gravitational potential. With this mask we get rid of (very slow) radial flows near the mid-plane: since the density there is six orders of magnitude higher than the wind, a tiny radial velocity fluctuation could otherwise

TABLE 1
PROPERTIES OF THE FIDUCIAL MODEL

Item	Value
Radial domain	$2 \text{ AU} \leq r \leq 100 \text{ AU}$
Latitudinal domain	$0 \leq \theta \leq \pi/2$
Resolution	$N_{\log r} = 256, N_{\theta} = 128$
Stellar mass	$1.0 M_{\odot}$
M_{disk}	$0.03 M_{\odot}$
Mid-plane density	$10^{10}(R/100 \text{ AU})^{-2.25} \text{ cm}^{-3}$
Mid-plane temperature	$20(R/100 \text{ AU})^{-0.5} \text{ K}$
Luminosities [photon s^{-1}]	
7 eV (“soft” FUV)	4.5×10^{42}
12 eV (LW)	1.6×10^{40}
25 eV (EUV)	5.0×10^{40}
1 keV (X-ray)	1.6×10^{39}
Initial abundances [n_X/n_H]	
H ₂	0.5
He	0.1
H ₂ O	1.8×10^{-4}
CO	1.4×10^{-4}
S	2.8×10^{-5}
Si	1.7×10^{-6}
Fe	1.7×10^{-7}
Gr	1.0×10^{-7}
Dust/PAH properties	
r_{dust}	5 Å
ρ_{dust}	2.25 g cm^{-3}
$m_{\text{dust}}/m_{\text{gas}}$	7×10^{-5}
σ_{dust}/H	$8 \times 10^{22} \text{ cm}^2$

give a spurious contribution to the mass-loss rate. As displayed in Fig. 1, the streamlines terminate on the disk at the surface where \mathcal{B} becomes negative. We consider this surface to be the base of the wind. (As discussed in §5.2, this definition of the wind base differs from that of GH09.)

Fig. 2 shows several flow variables along two representative streamlines originating from cylindrical radii $R \equiv r \sin \theta = 5 \text{ AU}$ and $R = 15 \text{ AU}$.

The density and temperature profiles shown by Fig. 1 can be divided into three relatively distinct regions:

- Midplane layer: $0 < (z/R) \lesssim 0.3$ ($R = r \sin \theta$ being cylindrical radius), $T < 10^2 \text{ K}$. The structure here is basically unchanged from the initial conditions.
- Intermediate layer: $0.3 \lesssim (z/R) \lesssim 0.6$, $10^{-19} \text{ g cm}^{-3} \lesssim \rho \lesssim 10^{-16} \text{ g cm}^{-3}$, $10^2 \lesssim T \lesssim 10^3 \text{ K}$. The total mass in this layer is $\sim 10^{-6} M_{\odot}$. EUV photons scarcely penetrate this region, whose properties are controlled by FUV and X-ray processes: photodissociation and photoelectric heating, as well as radiative cooling by collisionally excited molecular and/or atomic transitions. Most H₂ molecules and a lot of CO molecules survive in this region because of significant self- and cross-shielding of Lyman-Werner photons. Soft FUV photons that do not interact much with molecular hydrogen are relatively unshielded and pervade the intermediate layer, photodissociating OH and

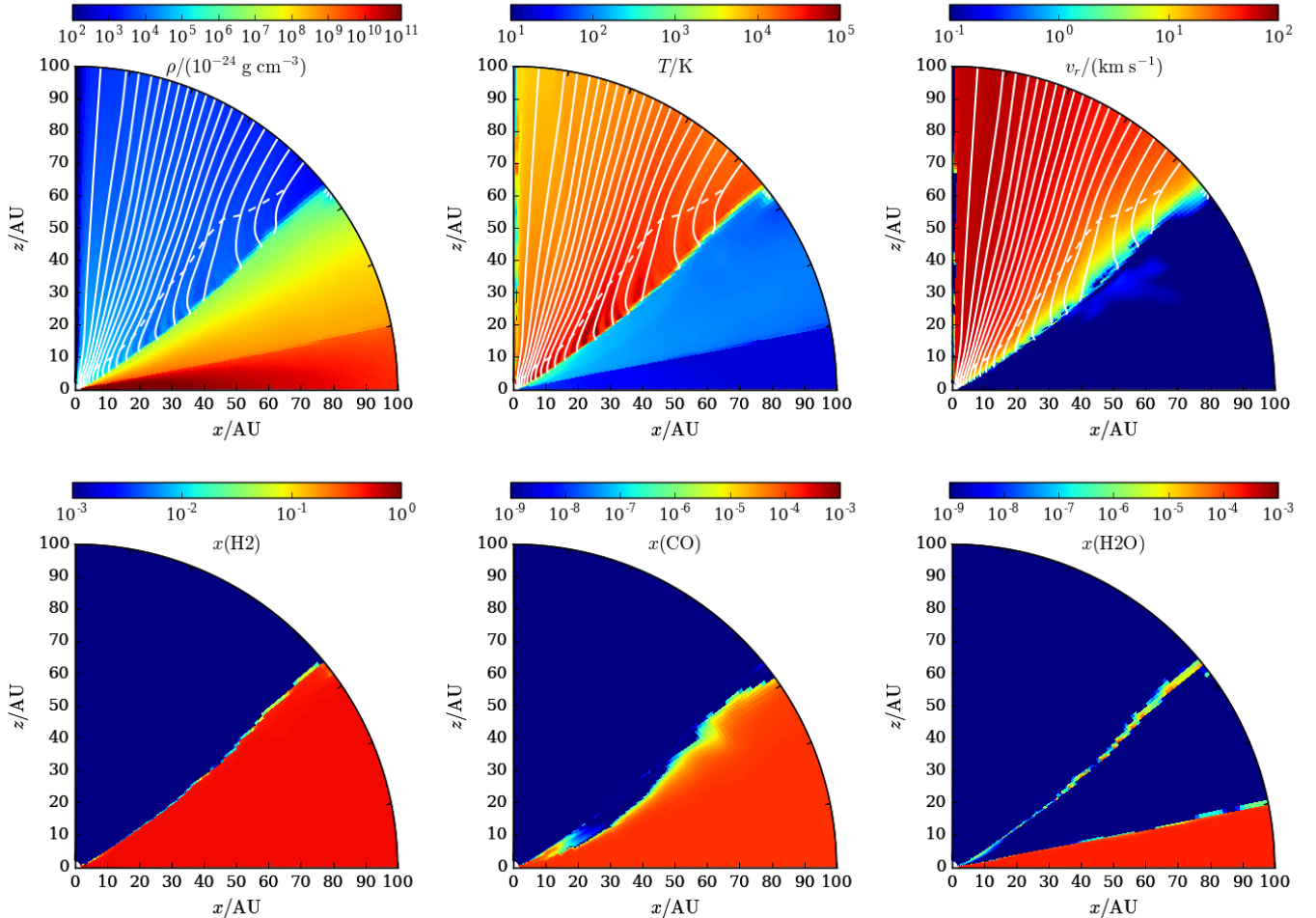


FIG. 1.— Meridional plots for the fiducial model (§3), averaged through the final 100 yr of the simulation. **Top row**: basic hydrodynamic profiles; left panel: mass density in units of 10^{-24} g cm $^{-3}$; middle panel: temperature in Kelvin; right panel: radial velocity in km s $^{-1}$. Panels in the top row are overlapped by streamlines (white solid lines), separated by $10^{-10} M_{\odot}$ yr $^{-1}$ wind mass loss rate (see §4.1 for details), and the locations of sonic points (white dashed line). **Bottom row**: relative abundance of different species [in units of $n(X)/n_{\text{H}}$]; left panel: H $_2$; middle panel: CO; right panel: H $_2$ O.

H $_2$ O), penetrating to the bottom of the layer, or escaping through the outer radial boundary.

- Wind layer: (z/R) \gtrsim 0.6, $\rho \lesssim 10^{-19}$ g cm $^{-3}$, $T \gtrsim 10^4$ K. This region is filled with mostly ionized gas, flowing outwards at radial velocity $v_r \sim 30$ km s $^{-1}$. Photoionization heating and adiabatic expansion dominate the thermodynamics of this region.

If we integrate the \mathcal{B} -masked radial mass flux at the the $r = 100$ AU boundary (and its reflection at $z < 0$) and average over the last 100 yr of our fiducial run, we obtain a total mass-loss rate $\dot{M}_{\text{wind}} \simeq 3.4 \times 10^{-9} M_{\odot}$ yr $^{-1}$, corresponding to a disk dispersal timescale $\sim 10^7$ yr. The mass-loss rate is lower than that of GH09 (see §5.2 for further discussion). However, our mass-loss rate undergoes significant fluctuations, and is uncertain to at least ~ 10 per cent. Fig. 3 plots the mass-loss rate for the last 200 yr of the (lower resolution) fiducial run (Model 0). They correlate with what appears to be a thermal instability of the outer disk, whereby it swells vertically, intercepts more radiation, and then swells further but also migrates

at a few km s $^{-1}$ through the outer boundary, temporarily increasing \dot{M} . This behavior is smoothed over by the time averages used to make Fig. 1. These swellings, being slower and denser than the general wind, partly shield themselves against photodissociation of some molecules, especially H $_2$ and CO, so that those molecules survive farther into the outflow than they would otherwise.

Even outside these swellings, there are also molecules surviving in regions with rather high temperature ($\sim 10^3$ K, or even up to $\sim 10^4$ K). H $_2$ O and OH molecules exist at the surface of the intermediate layer, detached from the midplane (last panel of Fig. 1). The reformation rates of H $_2$ O and OH are comparable to photodissociation at that surface. At the cooler temperatures below it, inside the intermediate layer, reformation is less efficient but photodissociating FUV is still present. The wind region, on the other hand, does not have sufficient H $_2$ (reactions that are most efficient in forming H $_2$ O and OH need H $_2$ as reactants, while the reactions that convert atomic H to OH and H $_2$ O are very slow).

In Fig. 4, we plot the distribution of CO, OH and H $_2$ O

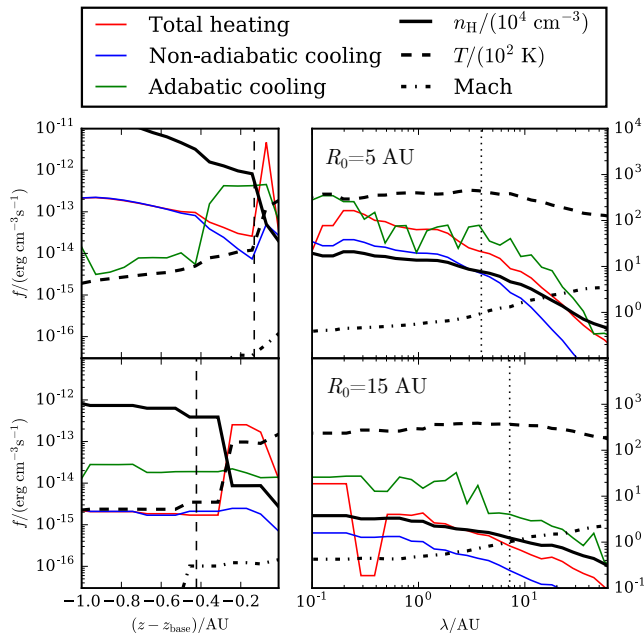


FIG. 2.— Cooling/heating rates (left ordinate) and fluid properties (right ordinate) along streamlines. n_{H} is the number density of hydrogen nuclei. In right column, horizontal axis is arc length (λ) measured from the wind base [where $\mathcal{B} = 0$, eq. (3)]. Vertical dotted line marks sonic point. Left column present the profile vertically below wind base (i.e. $z - z_{\text{base}}$). Vertical dashed line indicates wind base as defined by GH09. Upper row: streamline rooted at $R_0 = 5$ AU. Lower row: $R_0 = 15$ AU.

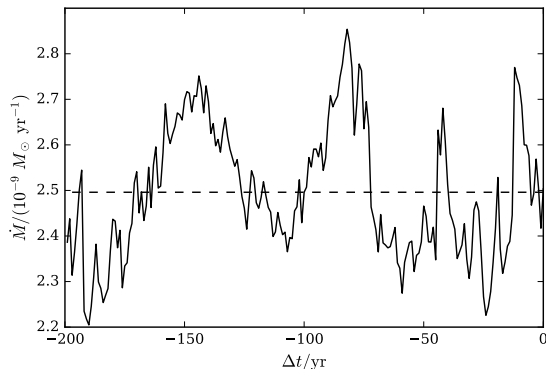


FIG. 3.— Variation of mass-loss rate measured at the $r = 100$ AU outer boundary of the fiducial model (Model 0). The dashed horizontal line shows the average of mass-loss rate over the last 200 yr.

in the wind region and intermediate layer, in the plane of by $\log_{10} T$ and v_r . (The temperature T here represents the kinetic temperature of the local (mostly H & He) gas, not the vibrational or even rotational excitation temperature of the molecules.) For those molecules, a tail on the high temperature ($T \sim 10^3$ – 10^4 K) and intermediate radial velocity ($v_r \sim 5$ – 10 km s $^{-1}$) end of the 2-D distribution indicate their survival at the bottom in the wind region. Such hot molecular gas would be less prominent had we assumed local thermochemical equilibrium. For the luminosity in the LW and EUV bands of our fiducial model, it can be estimated that the timescale of CO photodissociation is ~ 0.1 yr at $r \sim 10$ AU. Given the speed of photoevaporative outflow, this timescale is sufficient for some CO to survive ~ 0.1 – 1 AU into the hot wind. These timescales are sensitive to radial distance (from the radiation sources), to the way photodissocia-

tion is modeled (see §2.3), and to the LW and EUV band luminosity. Observational constraints on such molecules could be an important check on these models, and might diagnose the role of UV in driving PPD winds.

4.2. Exploring the Parameter Space

To explore the effects of our input parameters, we have run a number of additional simulations, most differing from the fiducial run in one parameter. These models and some synoptic results are listed in Table 2. We discuss some of these models here, and others in §§5.2–5.3 in relation to the works by GH09 and OECA10.

In the fiducial model the luminosity in the Lyman-Werner band is tiny compared to that in soft ($h\nu < 11.3$ eV) FUV photons: around 0.35 per cent, using the 9000 K black body SED. However, as observed by e.g. Gullbring et al. (2000), the SED for FUV radiation is rather variable from object to object and often more luminous in the LW band than the black-body model adopted by GH08 and GH09. Hence we include a series of models, with 0 and 100 times the fiducial luminosity in the Lyman-Werner band, to cover this uncertainty. We also test 0 and 10 times EUV or X-ray luminosity to diagnose the impact of those photons that can ionize atomic hydrogen.

For very small grains such as our PAHs, the grain absorption cross section for FUV and EUV photons depends on total grain mass rather than grain area. We have a much smaller grain mass than GH09. Model 9 in Table 2 has double the dust radius ($r_{\text{dust}} = 10$ Å) and therefore eight times the dust mass at the same relative number density ($n_{\text{Gr}}/n_{\text{H}} = 10^{-7}$).

To test our truncation errors, we repeat the fiducial run at resolution 128×64 , i.e. coarser by $\times 2$ in both latitude and radius. This convergence test is run for much longer time period (~ 2000 yr) to better characterize fluctuations around the mean state.

Fig. 5 illustrates the hydrodynamic structure of a few representative models. These plots are based on time averages over 100 yr, so that the flow field is in approximate steady state. In the runs with $100\times$ LW photons (Model 2) or $10\times$ X-ray photons (Model 8), a thick neutral atomic layer exists at the top of the intermediate layer. In this layer, the temperature and sound speed reach a local maximum with respect to height or latitude, and significant outflows may occur. This causes the jagged shape of the sonic curves in the third and fourth panels.

Figs. 6 and 7 show the vertical distributions of heating and cooling mechanisms at $R = 15$ AU, a typical location where the outflow streamlines originate. The three layer structure (§4.1) is obvious in most of the models. Details of those structures vary with model parameters, with implications for the mechanisms responsible.

The panels of Fig. 6 convey some general impressions about the heating mechanisms. The vertical heating profile usually has two peaks: one at the bottom of the intermediate layer, the other at the top of it. Photoionization heating by the harder (EUV and X-ray) photons dominates, unless these photons are absent or are overwhelmed by photons in other bands (e.g. Model 2, $100\times$ LW photons; see discussions below). On the cooling side (Fig. 7), the OH and/or H $_2$ O ro-vibrational transitions and S I 25 μm transition dominate at the bottom of inter-

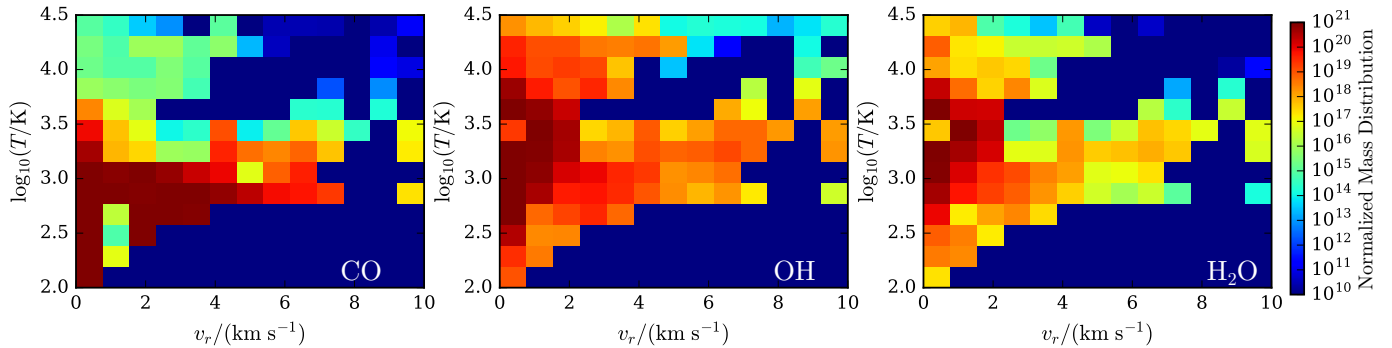


FIG. 4.— Distribution functions of key molecular species based on the fiducial model (left panel: CO; middle panel: OH; right panel: H₂O) in the two-dimensional space of $\{\log_{10} T\} \times \{v_r\}$ (common logarithm of temperature and radial velocity). The mass distribution function is normalized as $d^2m/[d\log_{10}(T/K)d(v_r/\text{km s}^{-1})]$, i.e. mass of the species per dex-temperature per $(v_r/\text{km s}^{-1})$.

TABLE 2
MODELS EXPLORING PARAMETER SPACE

No.	Description	\dot{M}_{wind} ($10^{-9}M_{\odot} \text{ yr}^{-1}$)	\dot{M}_{GH} ($10^{-9}M_{\odot} \text{ yr}^{-1}$)	Total heating (10^{30}erg s^{-1})	Efficiency	$\langle v_r \rangle$ (km s^{-1})
(1)	(2)	(3)	(4)	(5)	(6)	(7)
0	Fiducial	2.5 ± 0.2	11.6	4.4	0.67	39
1	No LW photons	2.5 ± 0.3	9.3	4.1	0.67	38
2	100× LW photons	17.6 ± 2.1	61.3	9.1	0.60	18
3	No "soft" FUV	1.1 ± 0.1	2.7	2.3	0.53	58
4	"Soft" FUV only	0.0	0.2	1.0	-	-
5	No EUV	0.0	3.7	1.6	-	-
6	10× EUV photons	9.4 ± 0.7	107.8	26.7	0.74	33
7	No X-ray	2.1 ± 0.2	6.9	2.6	0.80	38
8	10× X-ray photons	9.1 ± 0.4	55.6	14.1	0.42	24
9	$r_{\text{dust}} = 10 \text{ \AA}$	2.8 ± 0.6	10.5	3.5	0.68	30
10	OECA10 analog [†]	11.2 ± 4.2	105.0	0.8	0.54	5
11	Convergence test	2.7 ± 0.6	16.1	3.0	0.58	32

NOTE. — (1) Model identifier. (2) Parameter by which model differs from fiducial. (3) Wind mass-loss rate. The error quoted error is $\Delta\dot{M}_{\text{wind}} = \langle [\dot{M}(t)]^2 \rangle - \langle \dot{M} \rangle^2$, where the time averages are taken over the last 100 yr. (4) Estimated wind mass-loss rate using GH09 scheme. (5) Total radiative plus thermal-accommodation heating of the gas (note that the accommodation heating can be negative). (6) Thermal-to-mechanical conversion efficiency: $(\text{heating} - \text{non-adiabatic cooling})/(\text{heating})$. (7) Mean outflow velocity weighted by radial mass flux. †: Bernoulli parameter mask not applied; significant outflow occurs in the intermediate layer with $\mathcal{B} < 0$.

mediate layer, the Si II 35 μm and O I 63 μm transitions in the middle of that layer, and H₂ ro-vibrational cooling near the top. In the “wind” region, cooling and heating are dominated by recombination and the photoelectric effect. Using the integrated cooling rate, we have estimated some of the important line luminosities (Table 3).

5. DISCUSSION

5.1. Roles of different bands of radiation

The heating and thickness of the intermediate layer is mainly attributable to photons that penetrate a radial column $\gtrsim 10^{21} \text{ cm}^{-2} \sim 10^8 \text{ cm}^{-3} \times 10 \text{ AU}$, viz. soft FUV and X-rays. These two components penetrate to $n \sim 10^8 \text{ cm}^{-3}$, which approximately defines the top of the midplane layer. Scattered Ly α photons would penetrate to vertical columns $\sim 10^{22} \text{ cm}^{-2}$ if they were included (see Bethell & Bergin 2011).

Heating processes inside the intermediate layer do not directly contribute to the outflows. This is suggested in Fig. 1 by the terminations of the streamlines, which mark the surface where $\mathcal{B} = 0$, at the top of the intermediate layer; and also by the mass-loss rates in Table 2, especially for models 5 (soft FUV only), 6 (no EUV photons), and and 3 (no soft FUV). The relatively high density in

the bulk of the intermediate layer ($n \gtrsim 10^6 \text{ cm}^{-3}$) causes cooling processes to offset much of the radiative heating there. Nevertheless, the FUV photons, and in most cases the X-ray photons also, contribute indirectly to the mass-loss rate by thickening the intermediate layer, which exposes its upper surface to more intense EUV heating.

The LW photons play a more direct role. Due to self-shielding of H₂, heating by LW photons extends only slightly below the upper surface of the intermediate layer. These photons contribute dramatically to the total outflow. Admittedly, this is not convincingly shown by Table 2 alone: compare Models 0 (fiducial), 1 (no LW photons) and 2 (10× LW photons). In these three cases, the luminosities in the LW band are smaller than the EUV component. But the corresponding panels of Fig. 6 reveal a clear trend of increasing heating by H₂ pumping (see Appendix A.1). Model 2 (100× LW photons) clearly demonstrates that LW heating by interaction with H₂ can dominate the outflow when the LW is sufficient. It is worth noting that, for Model 2, the outflow velocity is approximately $\sim 1/3$ that of Models 0, 1, and 2: LW photons deposit less energy per reaction than EUV and X-ray (see also §2.3 and Appendix A.1), thereby heating the gas to a lower temperature and hence accelerating

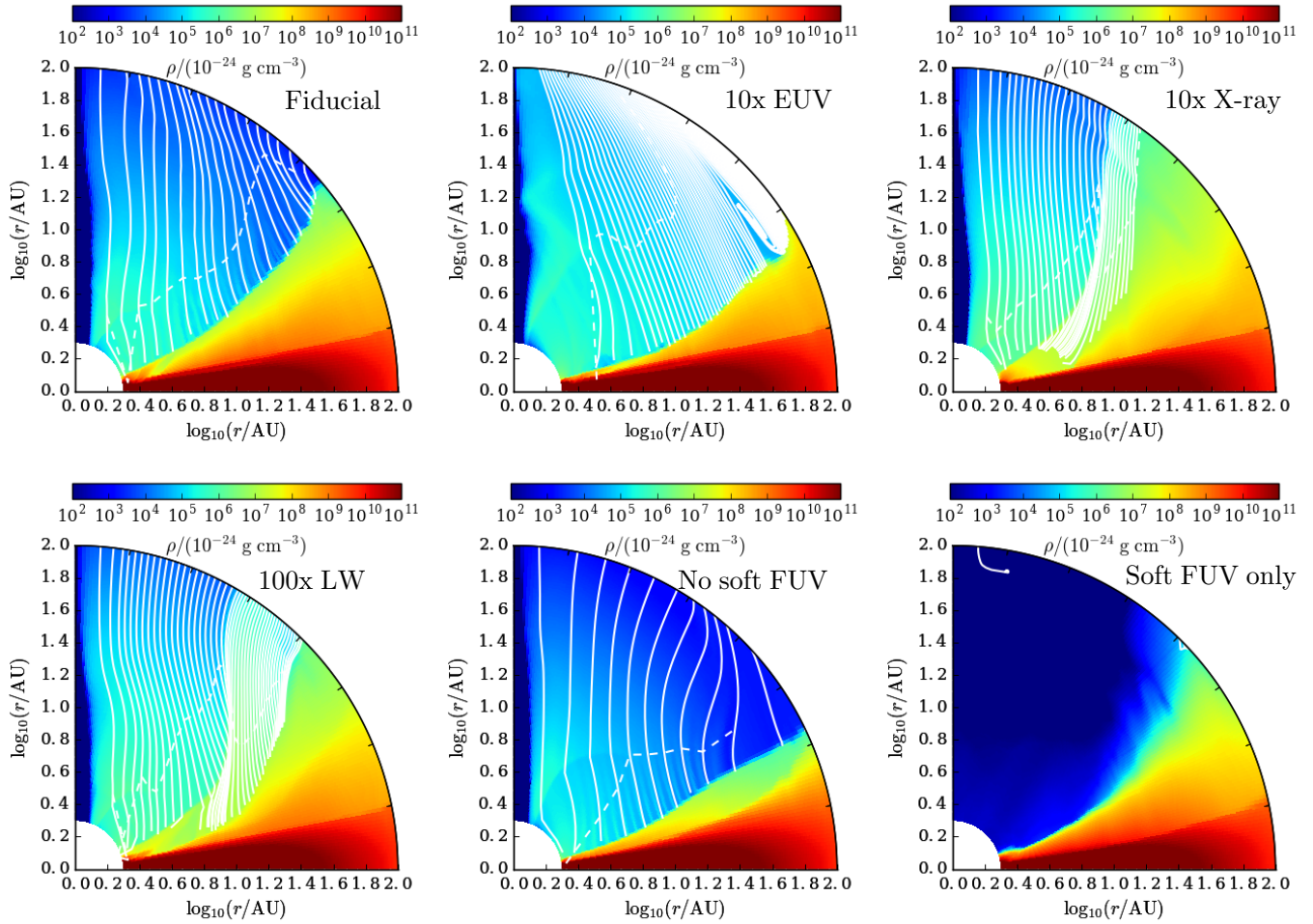


FIG. 5.— Selected plots of streamlines (based on 100 yr average), overlaid on density colormaps, that are relevant to the discussions in §4. The black curves, showing the streamlines, are separated by $10^{-10} M_{\odot} \text{ yr}^{-1}$ each. The white curves denote the location of sonic point of all streamlines plotted. Note that, for clearer presentation, the radial coordinates in all panels are $\log_{10}(r/\text{AU})$.

TABLE 3
APPROXIMATE LINE LUMINOSITY

Model	O I 63 μm	O I 6300 \AA	Si I 25 μm	Si II 35 μm	H ₂ ro-vib	OH/H ₂ O ro-vib	CO ro-vib
0	-4.31	-7.36	-4.00	-5.65	-4.67	-4.29	-3.89
1	-4.34	-8.17	-3.96	-5.73	-4.60	-4.36	-3.90
2	-3.75	-4.69	-4.17	-4.73	-4.11	-3.57	-3.91
3	-5.05	-7.72	-5.05	-6.48	-5.26	-3.61	-5.68
4	-5.05	-	-4.68	-	-5.61	-4.30	-4.26
5	-4.22	-7.31	-3.97	-5.58	-5.03	-4.63	-3.88
6	-4.43	-7.13	-3.88	-5.36	-3.65	-3.56	-3.78
7	-4.74	-8.02	-4.61	-6.30	-4.72	-4.26	-4.23
8	-3.57	-5.99	-3.11	-4.69	-4.15	-3.38	-3.37
9	-4.47	-4.94	-4.39	-5.94	-4.39	-4.07	-4.59
10	-4.38	-6.88	-	-4.55	-	-	-
11	-4.49	-5.24	-4.32	-5.98	-4.79	-4.94	-4.83

NOTE. — All luminosities are presented in $\log_{10}(L/L_{\odot})$.

the outflow to a lower velocity.

EUV photons are absorbed by a rather small column density ($\sim 10^{18} \text{ cm}^{-2}$) of neutral or molecular hydrogen. However, if they make their way to the surface of intermediate layer, EUV photons tend to dominate the photoevaporative outflow. This point is illustrated by comparison of Model 0 (fiducial) with 6 (no EUV) and 7 ($10\times$ EUV): Model 5 has its outflow almost totally shut down, while Model 6 has a dramatically increased mass loss rate and radial flow velocity. Because the EUV heating is concentrated in relatively little mass, it produces a high sound speed and therefore a relatively fast wind.

Since the X-rays have considerably larger penetration than LW and EUV photons, in fact comparable to that of the softer FUV photons, they deposit most of their heat in the intermediate layer, where cooling mechanisms remove energy efficiently from the gas. The exception among the cases in Table 2 is Model 8 ($10\times$ X-ray), where X-rays drive a substantial wind by themselves. Note that the wind velocity is about half that of the fiducial model because the heating is distributed over a larger mass. X-ray driving is further discussed below in connection with the work of Owen et al. (2010).

5.2. Comparison with GH09

Although we have modeled our fiducial case on that of GH09, our mass-loss rate is a few times smaller than theirs. GH09 did not simulate the hydrodynamic flow in two dimensions as we have done, but instead estimated \dot{M} by analytically matching their heated disks onto a spherical Parker wind. The fourth column of Table 2 shows the rates that would be estimated by applying their prescription to our heated disks. For the fiducial case, this estimate matches GH09's results fairly well, as determined by integrating their radius-dependent mass-loss rate from 1 through 100 AU. The latter agreement suggests that our simplified thermochemical network is sufficient to predict the temperature, density, and flow, if not all of the trace species and line emission that one would like to compare with observations. The differences between the third and fourth columns point to the importance of modeling the hydrodynamics properly, however. Fig. 8 shows the radial profiles of the mass-loss computed in these two different ways, and also for GH09's original model disk. Note that the latter extended beyond 100 AU.

GH09's analytic prescription computes the mass-loss rate as if the disk atmosphere, which in their models is hydrostatic, belonged to a spherical Parker wind with constant sound speed, i.e. an adiabatic wind with an isothermal equation of state. For each cylindrical radius R , the matching point between the hydrostatic atmosphere and the isothermal wind are chosen at such an altitude as to maximize the imputed mass-loss rate. This is how GH09 determine the wind base, $z_b(R)$. The sound speed of the wind is then the sound speed of the hydrostatic atmosphere at $z = z_b$. Note that \dot{M} —or rather $2\pi R^2 \dot{\Sigma}(R)$ —can be expected to have such a maximum with respect to the matching altitude z_b because of the strong vertical gradients of temperature and density within the atmosphere.

To understand better why our mass-loss rates differ from GH09's prescription, consider the streamline start-

ing from $R_0 = 15$ AU in Fig. 1 (see also the lower panel of Fig. 2). Using the density and temperature profiles obtained by our fiducial simulation, the density and temperature at the wind base (defined in the manner of GH09) read $n_H \simeq 3.7 \times 10^6 \text{ cm}^{-3}$ and $T \simeq 0.7 \times 10^3$ K. These values are in good agreement with figure 1 in GH09. The corresponding isothermal sound speed is $c_s \simeq 2.1 \text{ km s}^{-1}$: the hydrogen is atomic and neutral, with mean mass per particle $\bar{m} \simeq 1.3m_H$. The implied sonic radius is then $r_s \simeq 78$ AU, and the predicted density there is $n_{H,s} \simeq 10^5 \text{ cm}^{-3}$. The corresponding mass-loss rate for a spherical isothermal wind with these sonic-point parameters would be $\dot{M} \sim 2\pi r_s^2 \bar{m} n_{H,s} c_s \simeq 7 \times 10^{-9} M_\odot \text{ yr}^{-1}$. This is identified with the local mass-loss rate per logarithmic radius at the surface of the disk, viz. $2\pi R^2 \dot{\Sigma}$.

However, in the simulation, the actual sonic point on this streamline lies at $r_s \simeq 23$ AU. The actual density there is $n_{H,s} \simeq 1.2 \times 10^4 \text{ cm}^{-3}$, and the temperature is nearly 3.6×10^4 K, so that the gas is largely ionized ($\bar{m} \simeq 0.64 m_H$). The isothermal sound speed based on this temperature and molecular weight is $c_s \simeq 20 \text{ km s}^{-1}$. The corresponding $\dot{M} \approx 0.8 \times 10^{-9} M_\odot \text{ yr}^{-1}$ (again, this is indeed $2\pi R^2 \dot{\Sigma}$). This is about one order of magnitude less than GH09's prescription.

In short, the actual mass-loss rate is smaller than GH09's prescription by approximately the reciprocal of the ratio of sound speeds (and hence flow velocities): 2.1 km s^{-1} vs. 20 km s^{-1} . The wind thrusts—momentum flux $2\rho_s c_s^2$ times $4\pi r_s^2$ —are nearly equal. The thrust is necessarily limited by the pressure of the gas at the wind base, since the disk must support the force exerted on it by the escaping wind. Although we and GH09 define the wind bases separately, the pressures are similar because the bases are separated vertically by only $\sim 0.5 \text{ AU}$ out of $\sim 9 \text{ AU}$. An analogy can be made here with rocketry: at fixed thrust, the mass-flow rate in the rocket exhaust is inversely proportional to the exhaust velocity, or equivalently, to the specific impulse. By assuming a constant sound speed from their wind base upward, GH09's prescription fails to account for the increase in specific impulse due to the sharp rise in temperature above the wind base, even though this rise is also seen in their own hydrostatic disk atmospheres (see Fig. 1 of GH08).

5.3. Comparison with OECA10

GH09 found that X-rays made a significant but not dominant contribution to the mass-loss rate. OECA10, on the other hand, modeled photoevaporation driven solely by X-rays, with a full axisymmetric hydrodynamic treatment similar to our own, though with a simplified prescription for the gas temperature. OECA10 assumed an X-ray luminosity close to that of our fiducial model, without FUV or EUV, but found a higher a wind mass-loss rate $\sim 1.4 \times 10^{-8} M_\odot \text{ yr}^{-1}$. Although our fiducial model has comparable X-ray and EUV luminosities, ($L_X = 10^{30.4} \text{ erg s}^{-1}$, $L_{EUV} = 10^{30.3} \text{ erg s}^{-1}$) EUV appears to dominate the mass loss. When we turn off the EUV, our mass-loss rate becomes less than $10^{-10} M_\odot \text{ yr}^{-1}$ (Model 5 in Table 2). We have investigated the causes of these large differences.

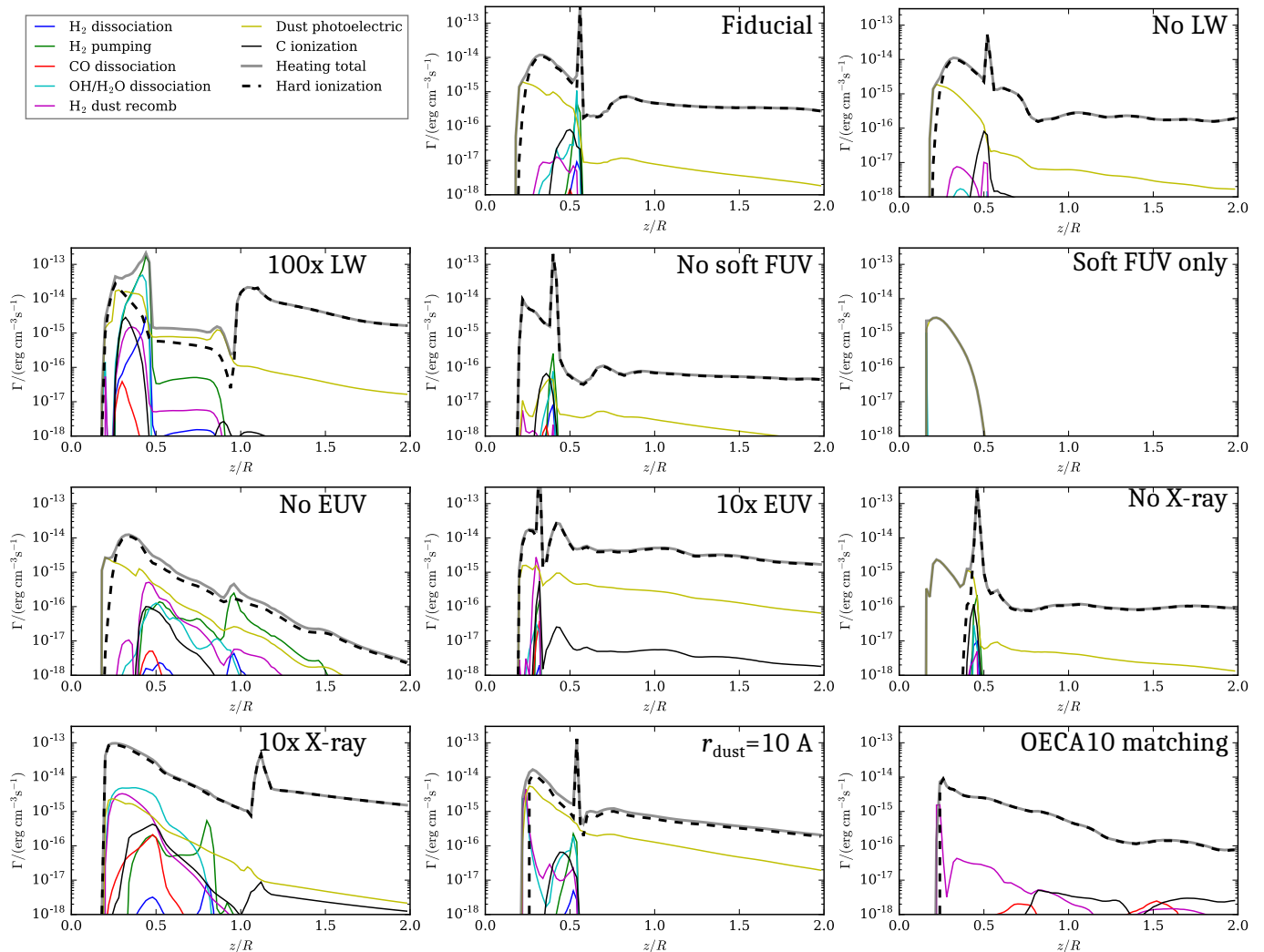


FIG. 6.— Profiles of heating mechanisms, in units of $\text{erg cm}^{-3} \text{s}^{-1}$, at $R = 15$ AU, for all models involved in this paper. Heating mechanisms are distinguished by line shape and color as marked in the legend at the upper left.

OECA10 prescribed the gas temperature as a function of the ionization parameter F_X/n_H , where F_X is the local X-ray flux, taking this relation from the hydrostatic models of Ercolano et al. (2008, hereafter EDRC08), who took $L_X = 2 \times 10^{30} \text{ erg s}^{-1}$ (very similar to ours), though with a slightly harder spectrum ($kT_X = 1.5 \text{ keV}$). As shown by Fig. 9, a similar correlation holds for our fiducial model, though with some spread around the mean relation. Recall however that EUV and FUV are also present in this model, and the former dominates at $T \gtrsim 10^4 \text{ K}$. At $T \approx 10^2\text{--}10^3 \text{ K}$, the regime of the intermediate layer, our mean $\xi - T$ relation falls somewhat below that of OECA10 by $\sim 0.2\text{--}0.5$ dex. We attribute this difference partially to the cooling mechanisms. The hydrostatic models of EDRC08 excluded cooling mechanisms by molecules and neutral atomic sulfur. In Table 3, we observe significant contribution to cooling by H_2O and neutral sulphur in the intermediate layer.

Adiabatic expansion also contributes to the differences between our $\xi - T$ relation and that assumed by OECA10. Comparing the corresponding panels in Fig. 2 shows that adiabatic expansion removes around 3/4 to 1/3 (the ratio varies from location to location) of the internal energy injected by heating (converting it to kinetic energy); ap-

plying the the hydrostatic $\xi - T$ relation to hydrodynamics assumes that this part of the energy still contributes to the gas temperature, and hence counts this part of the energy twice.

Perhaps the dominant difference between our model and that of EDRC08, however, involves the dust. Our recipes for thermal accommodation per gas-dust collision are identical to theirs (see Appendix A.3.3). Our dust-to-gas ratio ($\sim 10^{-4}$) is smaller than theirs (6.5×10^{-4}). However, EDRC08 assumed an MRN size distribution of dust grains (Mathis et al. 1977). The present work assigns a very small radius to all grains (5 \AA). This results in a dust surface area per gas mass that is ~ 10 times larger than in EDRC08, with a corresponding increase in the rate of cooling by thermal accommodation.

In support of the arguments here, we have run Model 10 (Table 2), in which all cooling processes related to molecules and neutral sulphur are disabled, the abundance of PAHs is lowered by $\times 10^{-1}$, and X-rays are the only hard photons (no EUV or FUV). This model yields a mass-loss rate of $\sim 1.1 \times 10^{-8} M_\odot \text{ yr}^{-1}$, fairly close to the results in OECA10.

6. CONCLUSIONS

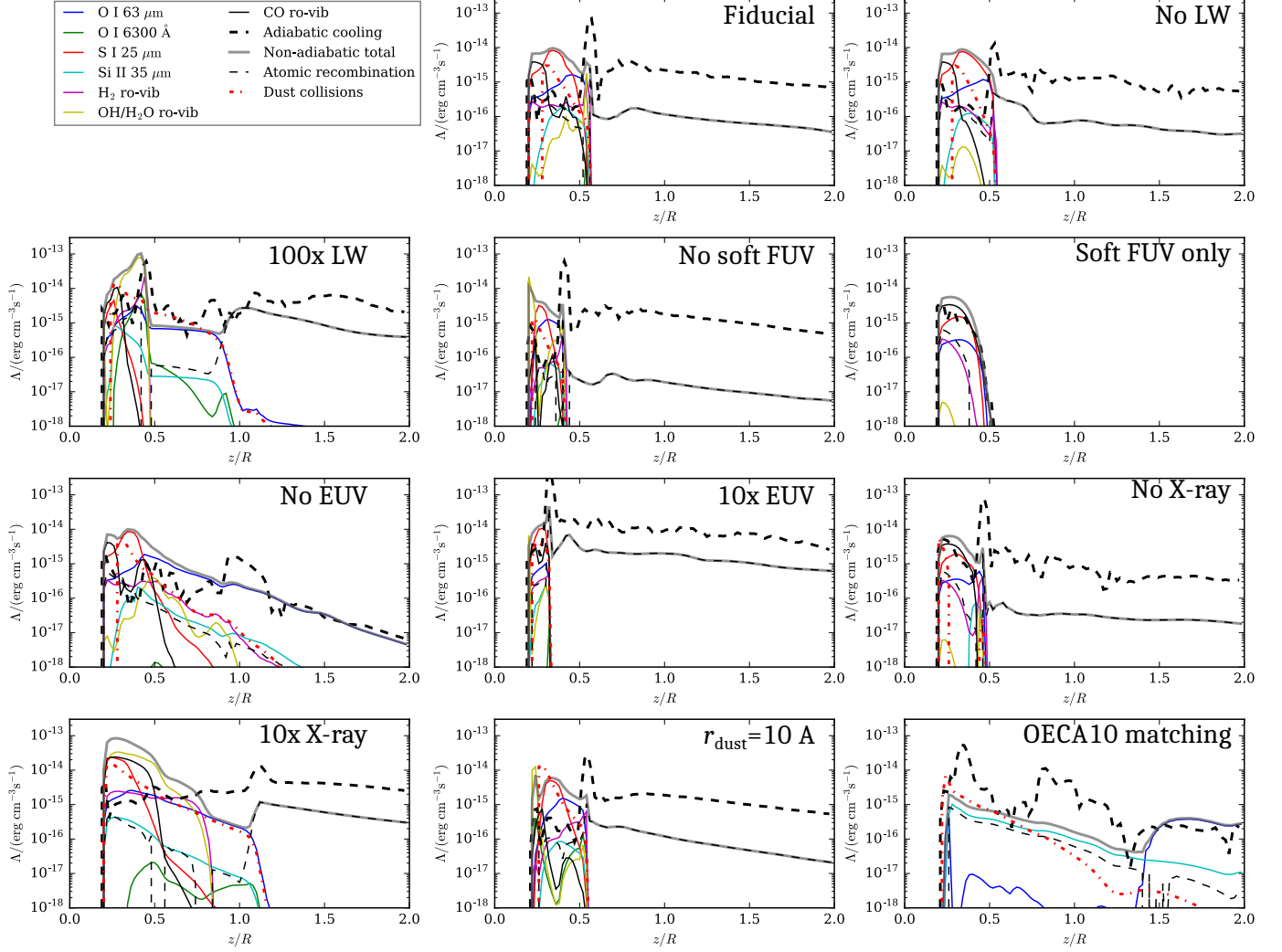


FIG. 7.— Same as Fig. 6, but shows profiles of different cooling mechanisms at $R = 15$ AU.

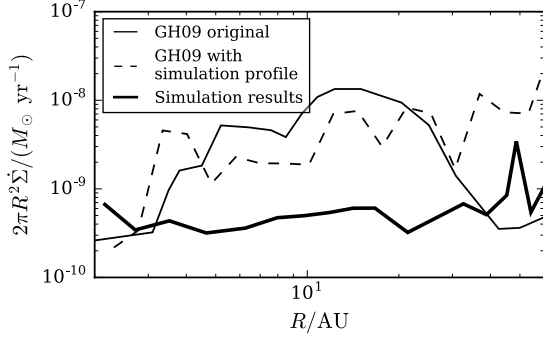


FIG. 8.— Radial profiles of the differential wind mass loss rate, ($2\pi R^2 \dot{\Sigma}$), for the time-averaged fiducial simulation. Dashed curve is calculated by applying GH09’s prescription to the density and temperature structure of our simulation, whereas solid curve is our actual mass-loss rate.

In summary, this work combines hydrodynamics with consistent ray-tracing radiative transfer and thermochemistry to study the photoevaporation mechanisms of protoplanetary disks. Irradiated by the FUV, EUV and X-ray radiation from the central source, the disk develops a three-layer structure; ordered by increasing latitude, these are a cold midplane region ($T < 10^2\text{K}$), a warm intermediate layer ($T \sim 10^2\text{--}10^3\text{K}$) and a hot

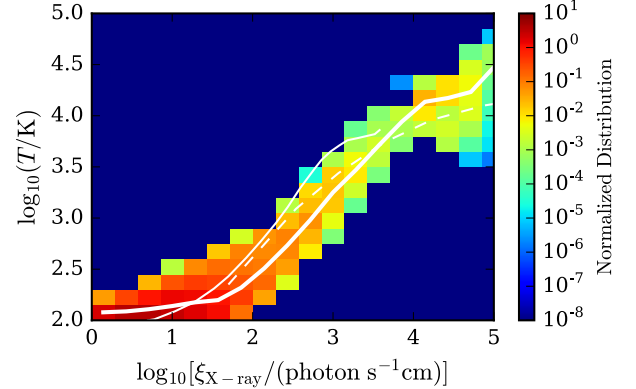


FIG. 9.— Distribution function of gas in the space spanned by $\{\log_{10} T\} \times \{\log_{10} \xi_{X\text{-ray}}\}$, measured for the fiducial model. X-ray ionization parameter $\xi_{X\text{-ray}}$ is defined as F_X/n_H , viz. photon number flux density divided by the number density of hydrogen nuclei. Heavy white curve indicates the $\log_{10} \xi\text{--}(\log_{10} T)$ relation based on our colormap histogram (the average of $\log_{10} T$ is weighted by the mass of gas), while the thin white curves indicate the hydrostatic $\xi\text{--}T$ relations adopted in OECA10 (solid: inner-hole disks; dashed: primordial disks; note that the definition of ξ is different in OECA10, which is converted here to the definition in this paper).

tenuous ionized wind ($T \gtrsim 10^4\text{K}$). The initial structure of the disk, the abundances and chemistry, and the amount and size of the dust, broadly follow GH09, but the time-averaged wind mass-loss rate is somewhat lower, $\dot{M}_{\text{wind}} (< 10 \text{ AU}) \approx 3.4 \times 10^{-9} M_{\odot} \text{ yr}$, and the typical radial velocity is higher $\sim 30 \text{ km s}^{-1}$, due in part at least to our explicit multidimensional modeling the hydrodynamics. Our solutions never reach a complete steady state, but show fluctuations ~ 10 per cent in \dot{M}_{wind} , which correlate with what appears to be an instability in the response of the upper part of the intermediate layer to irradiation. (The fluctuations might be smaller in three-dimensional simulations due to azimuthal averaging.) By varying the various hard-photon luminosities, we find that the most crucial factor to \dot{M}_{wind} is the total heating by radiation that interacts strongly with molecular and/or atomic hydrogen, viz. EUV and Lyman-Werner photons. Abundant soft FUV photons and X-rays also help in launching the wind by increasing the thickness of the intermediate layer, causing its upper surface to intercept more of the EUV. By comparison with previous work on PPD photoevaporation, we find that mass-loss estimates are sensitive to the fidelity of both the hydrodynamics and thermochemistry. Mass loss is also sensitive to intrinsically uncertain physical parameters, notably the dust abundance and size distribution. Some molecules, including OH, H₂O and CO, persist in the lower wind at higher temperatures and intermediate velocities than would be expected from equilibrium

chemistry, as a consequence of comparable hydrodynamic and (photo-)chemical timescales.

There are several aspects of the problem which we hope to explore in future work. Using post-processing of these hydrodynamic models, now that we have the temperature, density, and velocity structure, it should be possible to model molecular and atomic lines, including trace species not important for heating and cooling, and explicitly treating the level populations and optical depths of CO, etc. These lines and their profiles will be used to confront our photoevaporative models with observations, e.g. Carr et al. (2004); Carr & Najita (2008); Bast et al. (2011); Brown et al. (2013); Simon et al. (2016).

Eventually, we plan to add magnetic fields to the problem. These probably must be present to explain accretion, whether driven by MRI turbulence or by the wind itself. The FUV- and X-ray-heated intermediate layer, which is not hot enough to escape purely thermally, may well drive a denser, cooler, and higher- \dot{M} wind when coupled to the field (Bai et al. 2016).

This work was supported by NASA under grant NNX10AH37G and by Princeton University's Department of Astrophysical Sciences. We thank our colleagues Xuening Bai, Bruce Draine, Munan Gong, Eve Ostriker, James Owen, Kengo Tomida, and Zhaohuan Zhu, for discussions and for detailed comments on a preliminary draft. All errors are the responsibility of the authors, LW and JG.

REFERENCES

- Ádámkóvics, M., Glassgold, A. E., & Najita, J. R. 2014, *ApJ*, 786, 135, (**AGN14**)
- Alexander, R. D., Clarke, C. J., & Pringle, J. E. 2005, *MNRAS*, 358, 283
- . 2006a, *MNRAS*, 369, 216
- . 2006b, *MNRAS*, 369, 229
- Bai, X.-N., & Goodman, J. 2009, *ApJ*, 701, 737
- Bai, X.-N., Ye, J., Goodman, J., & Yuan, F. 2016, *ApJ*, 818, 152
- Bast, J. E., Brown, J. M., Herczeg, G. J., van Dishoeck, E. F., & Pontoppidan, K. M. 2011, *A&A*, 527, A119
- Bethell, T. J., & Bergin, E. A. 2011, *ApJ*, 739, 78
- Brown, J. M., Pontoppidan, K. M., van Dishoeck, E. F., et al. 2013, *ApJ*, 770, 94
- Carr, J. S., & Najita, J. R. 2008, *Science*, 319, 1504
- Carr, J. S., Tokunaga, A. T., & Najita, J. 2004, *ApJ*, 603, 213
- Chiang, E. I., & Goldreich, P. 1997, *ApJ*, 490, 368
- Draine, B. T. 2011, *Physics of the Interstellar and Intergalactic Medium* (Princeton University Press)
- Draine, B. T., & Bertoldi, F. 1996, *ApJ*, 468, 269
- Draine, B. T., & Sutin, B. 1987, *ApJ*, 320, 803
- Ercolano, B., Drake, J. J., Raymond, J. C., & Clarke, C. C. 2008, *ApJ*, 688, 398, (**EDC08**)
- Geers, V. C., van Dishoeck, E. F., Visser, R., et al. 2007, *A&A*, 476, 279
- Geers, V. C., Augereau, J.-C., Pontoppidan, K. M., et al. 2006, *A&A*, 459, 545
- Glover, S. C. O., Federrath, C., Mac Low, M.-M., & Klessen, R. S. 2010, *MNRAS*, 404, 2
- Goldsmith, P. F. 2001, *ApJ*, 557, 736
- Gong, M., Ostriker, E. C., & Wolfire, M. G. 2016, *ArXiv e-prints*, arXiv:1610.09023
- Gorti, U., & Hollenbach, D. 2008, *ApJ*, 683, 287
- . 2009, *ApJ*, 690, 1539
- Gullbring, E., Calvet, N., Muzerolle, J., & Hartmann, L. 2000, *ApJ*, 544, 927
- Haisch, Jr., K. E., Lada, E. A., & Lada, C. J. 2001, *ApJ*, 553, L153
- Haworth, T. J., Boubert, D., Facchini, S., Bisbas, T. G., & Clarke, C. J. 2016, *MNRAS*, 463, 3616
- Haworth, T. J., Facchini, S., Clarke, C. J., & Cleeves, L. I. 2017, *MNRAS*, 468, L108
- Haworth, T. J., & Harries, T. J. 2012, *MNRAS*, 420, 562
- Hindmarsh, A. C., Brown, P. N., Grant, K. E., et al. 2005, *ACM Transactions on Mathematical Software (TOMS)*, 31, 363
- Hollenbach, D., Johnstone, D., Lizano, S., & Shu, F. 1994, *ApJ*, 428, 654
- Hollenbach, D., & McKee, C. F. 1979, *ApJS*, 41, 555
- Igea, J., & Glassgold, A. E. 1999, *ApJ*, 518, 848
- Ilgner, M., & Nelson, R. P. 2006, *A&A*, 445, 205
- Kwan, J., & Krolik, J. H. 1981, *ApJ*, 250, 478
- Li, A., & Draine, B. T. 2001, *ApJ*, 554, 778
- Mathis, J. S., Rumpl, W., & Nordsieck, K. H. 1977, *ApJ*, 217, 425
- McElroy, D., Walsh, C., Markwick, A. J., et al. 2013, *A&A*, 550, A36
- Mignone, A. 2014, *Journal of Computational Physics*, 270, 784
- Nelson, R. P., Gressel, O., & Umurhan, O. M. 2013, *MNRAS*, 435, 2610
- Neufeld, D. A., & Kaufman, M. J. 1993, *ApJ*, 418, 263
- Owen, J. E., Ercolano, B., Clarke, C. J., & Alexander, R. D. 2010, *MNRAS*, 401, 1415, (**OECA10**)
- Perez-Becker, D., & Chiang, E. 2011, *ApJ*, 727, 2
- Shull, J. M. 1978, *ApJ*, 224, 841
- Simon, M. N., Pascucci, I., Edwards, S., et al. 2016, *ApJ*, 831, 169
- Tielens, A. G. G. M., & Hollenbach, D. 1985, *ApJ*, 291, 722, (**TH85**)
- van Dishoeck, E. F., & Dalgarno, A. 1984, *Icarus*, 59, 305
- Verner, D. A., Ferland, G. J., Korista, K. T., & Yakovlev, D. G. 1996, *ApJ*, 465, 487
- Verner, D. A., & Yakovlev, D. G. 1995, *A&AS*, 109
- Visser, R., van Dishoeck, E. F., & Black, J. H. 2009, *A&A*, 503, 323
- Weingartner, J. C., & Draine, B. T. 2001, *ApJS*, 134, 263
- White, C. J., Stone, J. M., & Gammie, C. F. 2016, *ApJS*, 225, 22
- Woitke, P., Riaz, B., Duchêne, G., et al. 2011, *A&A*, 534, A44

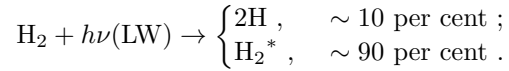
APPENDIX

A. DETAILS OF THERMOCHEMICAL PROCESSES

A.1. *FUV induced reactions of H₂*

When a 13.6 eV $> h\nu > 11.3$ eV photon (the ‘‘Lyman-Werner’’ band, or LW for short) encounters hydrogen molecules, this photon can be absorbed by a H₂ molecule, and excite the H₂ molecule into an excited electronic state. This state can spontaneously decay into different ro-vibrational states, hence we have to include the excited H₂^{*} as a representative for excited molecular hydrogen. Such photo-pumping of H₂ is also subject to self-shielding effects. We follow Draine & Bertoldi (1996) for the shielding factor.

As summarized by TH85, about 10 per cent of the excited hydrogen molecules result in photo-dissociation; we hereby simplify this reaction channel by adding a branch to the main photo-excitation channel, namely,



H₂^{*} molecules may also be directly photo-dissociated; the reaction cross section of TH85 is adopted. We take 0.4 eV as the amount of energy deposited in the gas as heat per FUV dissociation of H₂ (Gong et al. 2016; see also Hollenbach & McKee 1979).

At gas densities relevant here, the majority of excited hydrogen molecules are de-excited by collisions with other particles, especially H₂ or H. The de-excitation rate (with the $v = 6$ vibrational state as a proxy for all excited H₂^{*}), is estimated by (see also TH85),

$$\begin{aligned} k_{\text{de}}(\text{H}) &\simeq 1.8 \times 10^{-13} \text{ cm}^3 \text{ s}^{-1} \times \left(\frac{T}{\text{K}}\right)^{1/2} \exp\left(-\frac{1000 \text{ K}}{T}\right) ; \\ k_{\text{de}}(\text{H}_2) &\simeq 2.3 \times 10^{-13} \text{ cm}^3 \text{ s}^{-1} \times \left(\frac{T}{\text{K}}\right)^{1/2} \exp\left(-\frac{18000 \text{ K}}{T + 1200 \text{ K}}\right) . \end{aligned} \tag{A1}$$

Each collisional de-excitation deposits ~ 2.6 eV of heat into the gas (see also TH85). The rate for spontaneous radiative de-excitation of H₂^{*} is taken to be $A(\text{H}_2^*) \simeq 2 \times 10^{-7} \text{ s}^{-1}$ (TH85).

A.2. *FUV induced reactions of H₂O and OH*

Photodissociation of H₂O and OH is not drastically affected by self-/cross-shielding due to line overlap. For the photodissociation cross sections of these two species as functions of photon energy, we adopt Fig. 1 of AGN14. These reactions also heat the gas. Here we adopt the estimate in AGN14 that about $\sim 0.5(h\nu - E_{\text{diss}})$ of heat is deposited into the gas per reaction, where $E_{\text{diss}}(\text{H}_2\text{O}) \simeq 5.13$ eV, and $E_{\text{diss}}(\text{OH}) \simeq 4.41$ eV. Photodissociation of OH may result in oxygen atoms in the ¹D state, denoted by O^{*}, which spontaneously decays to the ³P state while emitting a photon at 6300 Å. Due to the uncertainty or variability of the FUV spectrum, we adopt the crude approximation that ~ 55 per cent of the OH dissociated results in O^{*} (van Dishoeck & Dalgarno 1984; Woitke et al. 2011). This seems not to be significant for hydrodynamics; nevertheless, as the [O I] 6300 Å radiation is an important diagnostic of PPDs winds, we expect this to be useful in our incoming analysis of comparison between simulation results and observations.

A.3. *Dust and PAH*A.3.1. *Dust-assisted H₂ formation*

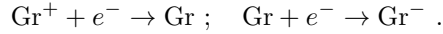
The reaction rate of H₂ formation on dust surface directly follows Bai & Goodman (2009), except for the efficiency of formation, for which we adopt the scheme of AGN14,

$$\eta \sim \begin{cases} 1 , & T_{\text{dust}} < 25 \text{ K} ; \\ 0.6 , & 25 \text{ K} < T_{\text{dust}} < 80 \text{ K} ; \\ 0.33 , & 80 \text{ K} < T_{\text{dust}} < 900 \text{ K} ; \\ 0 , & T_{\text{dust}} > 900 \text{ K} ; \end{cases} \tag{A2}$$

where T_{dust} is the dust temperature, which may be significantly different from the gas temperature T . A typical formation rate is $R \simeq 7.5 \times 10^{-17} \text{ cm}^3 \text{ s}^{-1}$ at 100 K, which is comparable to the value in photodissociation regions (PDRs) given the geometric dust cross section $8 \times 10^{-22} \text{ cm}^2$ per hydrogen nucleus (see §31.2 in Draine 2011). The formation of each H₂ molecules deposits ~ 1.5 eV of heat into the gas, the remaining recombination energy being radiated (AGN14). We take this effect into account.

A.3.2. Dust-assisted recombination and photoelectric effect

Dust-assisted recombination is implemented by including the following two processes:

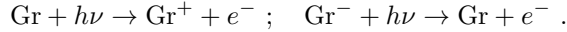


The efficiency of Gr and Gr^+ capturing free electrons follows the fitting formulae for electrostatic focusing in Draine & Sutin (1987) and the sticking probability evaluated by Weingartner & Draine (2001). The following two kinds of reactions close the cycle of dust-assisted neutralization:



Here X represents H, He, C, O, S, Si, or Fe. The rates of these reactions are evaluated using the same method as in Bai & Goodman (2009), using the desorption temperature summarized by Ilgner & Nelson (2006).

Photoelectric reactions of neutral and negatively charged dust grains are included,



The majority of the radiation absorbed is converted to dust thermal energy (which is in balance with thermal radiation of dust), but some is carried off by the photoelectrons. The cross section for photon absorption and photoelectric yield are evaluated based on the recipes elaborated in Li & Draine (2001) and Weingartner & Draine (2001). The work function is assumed to be $W \simeq 4.4$ eV (Weingartner & Draine 2001) for carbonaceous grains. The energy deposited into the gas per reaction is estimated by $(h\nu - W)$. Ideally, our treatment should involve the valence band ionization potential (Weingartner & Draine 2001), which differs from W by ~ 2 eV for $r_{\text{dust}} = 5$ Å particles (this difference is smaller for larger grains). However, for simplicity and because our very small grains are proxies for grains of all sizes, we omit this refinement.

A.3.3. Dust-gas energy transfer and artificial heating term

Near the midplane, the gas acquires energy and maintains temperature through the energy transfer with dust. The gas-dust energy transfer rate is estimated following Goldsmith (2001):

$$\Lambda_{\text{dust}} = \sum_{\text{sp}} n_{\text{sp}} \left(\frac{8k_{\text{B}}T}{\pi m_{\text{sp}}} \right)^{1/2} \sigma_{\text{dust}} \alpha \times 2k_{\text{B}}(T - T_{\text{dust}}) , \quad (\text{A3})$$

where the subscripts “sp” range over species, T is the gas temperature, T_{dust} the dust temperature, σ_{dust} is the geometric dust cross section, $\alpha \sim 0.5$ is the efficiency of gas-dust energy transfer (typically referred as the *accommodation coefficient*). It is possible that Λ_{dust} can be negative, indicating a heating instead of cooling process.

We further assume that the energy-transfer process does not affect the dust temperature profile. We do not evaluate the radiative transfer of diffuse infrared radiation inside the disk, which should properly determine the temperature of dust. In order to have a reasonable estimate of T_{dust} profile, we assume local equilibrium, and adopt the simplest dual-temperature profile proposed by Chiang & Goldreich (1997), using the following equation,

$$0 = \frac{d\epsilon_{\text{dust}}}{dt} = \max \left[4\sigma_{\text{B}}T_{\text{ah}}^4(R)\sigma_{\text{dust}}q(T_{\text{dust}}) , \sum_{h\nu} F_{\text{eff}}(h\nu)\sigma(h\nu) \right] - 4\sigma_{\text{B}}T_{\text{dust}}^4\sigma_{\text{dust}}q(T_{\text{dust}}) , \quad (\text{A4})$$

where σ_{B} is the Stefan-Boltzmann constant, T_{ah} the desired artificial heating temperature as a function of R (e.g. Chiang & Goldreich 1997, figure 4), σ_{dust} the geometric cross section of dust, and $q(T_{\text{dust}})$ the Planck-averaged emission efficiency as a function of black-body radiation field temperature [we evaluate this value with eq. (24.16) in Draine 2011], $F_{\text{eff}}(h\nu)$ the local effective irradiative radiation flux at photon energy bin $h\nu$ (see eq. 1), and $\sigma(h\nu)$ the effective absorption cross section (see Appendix A.3.2).]

Optical photons ($h\nu \lesssim 4.5$ eV), which we have not included in our simulations, should also affect dust temperature in the regions that those photons penetrate. Although the optical luminosity is generally ~ 100 times greater than all other bands combined, the dust temperature is rather insensitive to the inclusion of optical radiation because the thermal emission per grain $\propto T_{\text{dust}}^6$ (emissivity $q \propto T_{\text{dust}}^2$). We have conducted a test that includes an optical photon-energy bin with luminosity $2.34 L_{\odot}$ (see GH09), to find that the dust temperature in the intermediate layer rises by ~ 40 per cent, while the gas temperature there is almost invariant (as gas thermodynamics is dominated by processes not related to dust in the intermediate layer). As a result, the mass loss rate is unaffected by optical photons.

A.4. Other Molecular and Atomic Cooling Processes

A.4.1. Molecular ro-vibrational line cooling

Based on Neufeld & Kaufman (1993), ro-vibrational cooling caused by collisionally excited CO, OH, H_2O and H_2 are evaluated using interpolation tables. All of those cooling rate calculation schemes require the optical depth parameter \tilde{N}_{X} defined in Neufeld & Kaufman (1993), as a measure of escape probability of photons that remove energy from the gas, where X is the species interested, and \tilde{N}_{X} is the local $Gn(\text{X})/|\nabla v|$, where v is the local characteristic velocity, and G is a geometric factor at the order of 1; note that \tilde{N} has units of time/volume. Here we use $\tilde{N}_{\text{X}} \sim n(\text{X})/(v_{\text{th}}/h)$ to

estimate \tilde{N} , where h is the local scale height, and $v_{\text{th}} \simeq [2k_{\text{B}}T/m(X)]^{1/2}$ is the thermal speed of the species X: $n(X)h$ is a reasonable estimate of vertical column density integrated from $z = \infty$. In the regions where molecular cooling is important, the magnitude of the vertical gradient in the flow velocity is $\lesssim 10^{-1} \text{ km s}^{-1} \text{ AU}^{-1}$. This is comparable to but smaller than v_{th}/h , which is typically $10^{-1}\text{--}10^0 \text{ km s}^{-1} \text{ AU}^{-1}$ at the molecular weights and typical kinetic temperatures of relevant species. For simplicity, we use only the thermal speed for the optical depth parameter.

A.4.2. Atomic cooling processes

Collisionally excited atoms may decay radiatively, removing heat from the gas. In this work, we evaluate the cooling rate of atoms as follows. For each kind of atoms, we assume that they are in local statistical equilibrium and calculate the population fraction on the “upper levels” of transitions by taking collisional (de-)excitation, photon or chemical pumping, and spontaneous decay into account, by solving detailed balance equations. With the population number of excited coolants obtained, the cooling rate is calculated by $\Lambda = \beta n_{\text{coolant}}^* A$, where n_{coolant}^* is the number density of the desired coolant on the excited state, A the Einstein A coefficient, and β the escape probability. According to previous research work such as Kwan & Krolik (1981) β is a function of line-center optical depth τ_0 ,

$$\beta \simeq \begin{cases} \left[\tau_0 \pi^{1/2} \left(1.2 + \frac{\sqrt{\ln \tau_0}}{1 + \tau_0/10^5} \right) \right]^{-1}, & \tau_0 \gtrsim 1; \\ \frac{1 - \exp(-2\tau_0)}{2\tau_0}, & \tau_0 \lesssim 1. \end{cases} \quad (\text{A5})$$

We estimate τ_0 as a function of local thermal velocity, vertical column density (estimated by $n_{\text{tot}}h$, where h is the local scale height), line center wavelength, and oscillator strength (which can be directly inferred from A), as given by eq. (9.10) of Draine (2011). In this work, we include these atomic coolants: Ly- α , [C II] 158 μm , [O I] 63 μm , O I 6300 \AA (note that the excited state of oxygen atom for this transition is treated separately; see Appendix A.2), [S I] 25 μm , [Si II] 35 μm , [Fe I] 24 μm , and [Fe II] 26 μm . We adopt the data in table 4 of TH85 for those transitions.